



Cross-well seismic and electromagnetic tomography for CO₂ detection and monitoring in a saline aquifer



Gualtiero Böhm^a, José M. Carcione^{a,*}, Davide Gei^a, Stefano Picotti^a, Alberto Michelini^b

^a Istituto Nazionale di Oceanografia e di Geofisica Sperimentale (OGS), Borgo Grotta Gigante 42c, 34010 Sgonico, Trieste, Italy

^b Istituto Nazionale di Geofisica e Vulcanologia (INGV), Via di Vigna Murata, 605, 00143 Roma, Italy

ARTICLE INFO

Article history:

Received 23 December 2014

Received in revised form

6 May 2015

Accepted 11 June 2015

Available online 18 June 2015

Keywords:

Seismic tomography

Electromagnetic tomography

CO₂ detection

ABSTRACT

Geological storage is one of the solutions to avoid the emission of carbon dioxide to the atmosphere. This process requires a careful monitoring of the CO₂ bubble, which can be performed by means of seismic and electromagnetic (EM) methods, on the basis of seismic velocity, attenuation and electrical conductivity contrasts before and after the injection. A successful monitoring depends on many factors, for instance the depth and properties of the reservoir. To test the feasibility of detecting the gas, we have performed cross-well seismic and EM tomographic inversions on a synthetic data set generated from a realistic aquifer partially saturated with CO₂. We use two different algorithms based on traveltimes picks. The method is novel regarding the EM inversion. Besides seismic velocity and conductivity, we have also obtained the seismic quality factor by performing attenuation tomography based on the frequency-shift approach. The RMS differences between the inverted and true initial models show that the methodology (and the adopted acquisition geometry) allows us to obtain reliable results which agree well with the true petrophysical model. Moreover, we have used a forward optimisation method to recover saturation, porosity and clay content from the tomographic seismic velocities, Q values and electric conductivity, with errors less than 15%.

© 2015 Elsevier B.V. All rights reserved.

1. Introduction

Carbon dioxide is being injected worldwide in hydrocarbon reservoirs and saline aquifers as one of the solutions to the greenhouse effect (Arts et al., 2004). It is essential to monitor the diffusion and location of the CO₂ to predict and prevent any leakage to the atmosphere. To this purpose, the most used non-invasive techniques are seismic and electromagnetic surveys (e.g., Carcione et al., 2006; Norman et al., 2008; Bourgeois et al., 2009; Picotti et al., 2012). The process consists of periodically acquiring the data and performing inversions to obtain the seismic velocity and electrical conductivity and infer from these properties the CO₂ saturation by using appropriate rock-physics models. The combined use of the seismic and EM methods can give more reliable results if the interpretation is based on suitable cross-property relations between seismic velocity and conductivity (Carcione et al., 2007, 2012; Picotti et al., 2012). Existing wells may be used to perform cross-well repeated surveys and tomographic analysis of the recorded data, as successfully done by Saito et al. (2006) in

the Nagaoka site and Carcione et al. (2012). Xue et al. (2009) used time-lapse well-logging data including gamma-ray log, neutron log, and induction log during CO₂ injection tests in the Nagaoka site.

The EM method is a novel transient technique proposed in Carcione et al. (2012) and it is based on traveltimes picks of the EM signal in the log(*t*) domain, where *t* is the time variable. In this domain, the pick of the maximum amplitude is possible since diffusion fields resemble waves. Equivalently, the pick (traveltimes) can be obtained as the time that the first derivative of the field is zero (Yu and Edwards, 1997). An alternative picking method is given in Lee and Uchida (2005). To our knowledge, the only crosshole experiments somewhat related to this technique have been performed by Wilt et al. (1995). The method has not to be confused with electrical resistivity tomography (ERT) (e.g., Christensen et al., 2006; Picotti et al., 2013).

The integrated geological model constitutes a porous description of the geological formation, where grain properties, fluid types, porosity, clay content and permeability are explicitly considered, defining characteristic values of the electrical conductivity, seismic velocities and seismic quality factors, before and after the CO₂ injection. We then apply two different inversion algorithms to obtain the P-wave velocity and electrical conductivity (Michelini, 1995; Böhm et al., 2000) and seismic P-wave quality

* Corresponding author.

E-mail addresses: jcarcione@inogs.it (J.M. Carcione), alberto.michelini@ingv.it (A. Michelini).

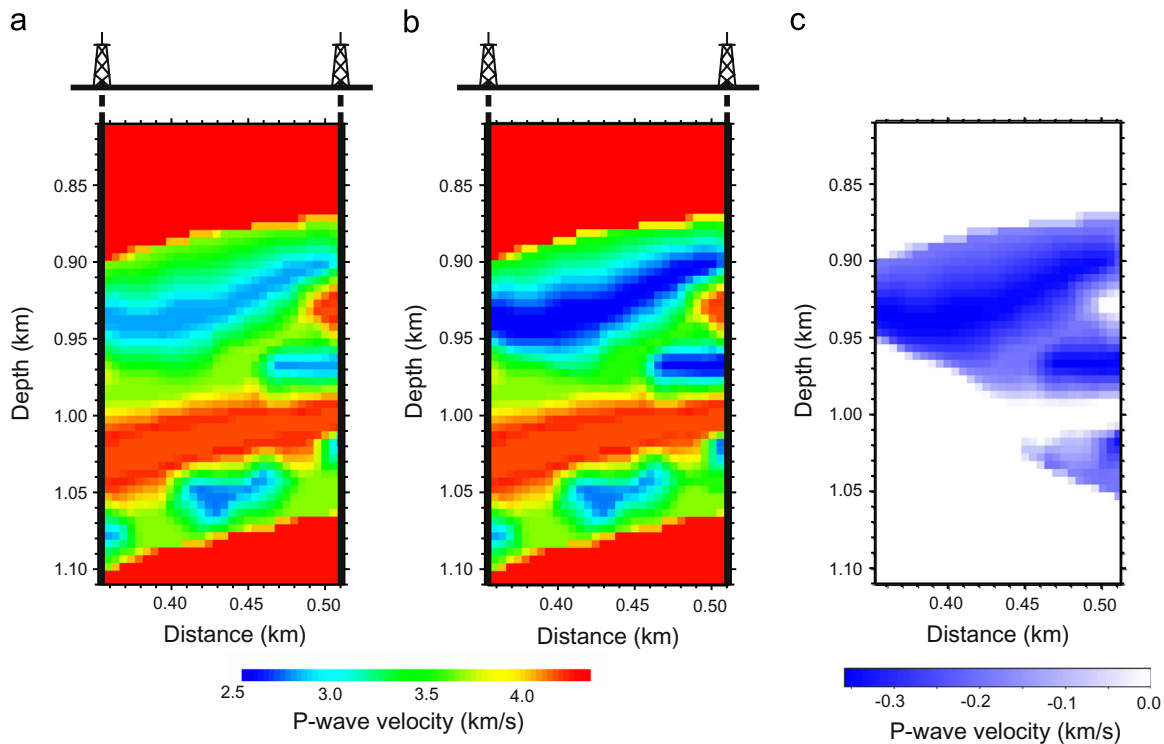


Fig. 1. P-wave velocity model before (a) and after (b) the CO₂ injection corresponding to the geological model defined in Carcione et al. (2012). Panel (c) shows the difference between panels (a) and (b). (For interpretation of the references to colour in this figure caption, the reader is referred to the web version of this paper.)

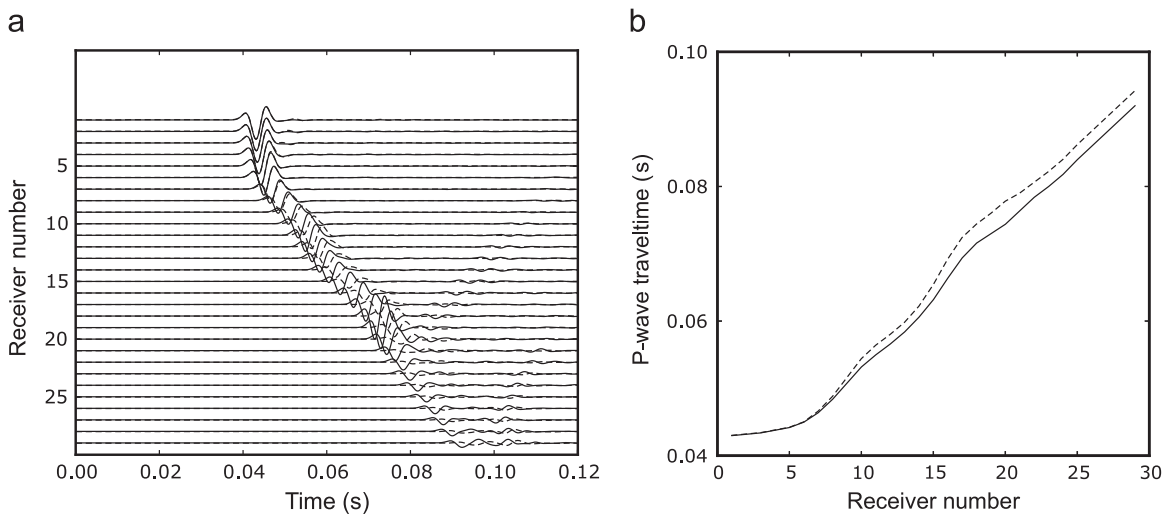


Fig. 2. Normalised seismic amplitude variation versus receiver number before and after the injection (solid and dashed curves, respectively) (a), and corresponding traveltimes (b). The source is located at the left well at a depth of 800 m and the vertical array of receivers is located at the right well (see Fig. 1).

factor, Q (Rossi et al., 2007; Picotti and Carcione, 2006).

In particular, Q has been recognised as a significant seismic indicator, which is not only useful for amplitude analysis and improving resolution, but also to obtain information on lithology, saturation, permeability and pore pressure (Best et al., 1994; Carcione et al., 2003; Helle et al., 2003; Carcione and Picotti, 2006). Hence, estimation of seismic attenuation is important as the estimation of interval velocities (Picotti et al., 2007). The attenuation tomographic algorithm adopted in this work (Rossi et al., 2007) is based on the frequency-shift approach, introduced by Quan and Harris (1997). The frequency-shift approach is based on the fact that, as the wavelet propagates within the medium, the high-frequency components of the spectrum decrease faster than the low-frequency components. As a result, the centroid of the signal

spectrum is downshifted to a lower frequency in the propagation from source to receiver. Under the assumption of a constant- Q model, this downshift is proportional to a linear integral of the attenuation along the ray path.

In this work, we perform tomographic inversions on seismic and EM data from a geological model of an aquifer generated with porous constitutive relations based on the White/CRIM theories of seismic velocity and electrical conductivity. The model has been generated in Carcione et al. (2012) and a data set of synthetic wave fields have been computed with direct methods to obtain the seismic and EM traveltimes. The model consists of a sandstone aquifer with shale intrusions, embedded in a shale formation. The model is two-dimensional, so if we assume that the plume extension in the direction normal to the section is 100 m,

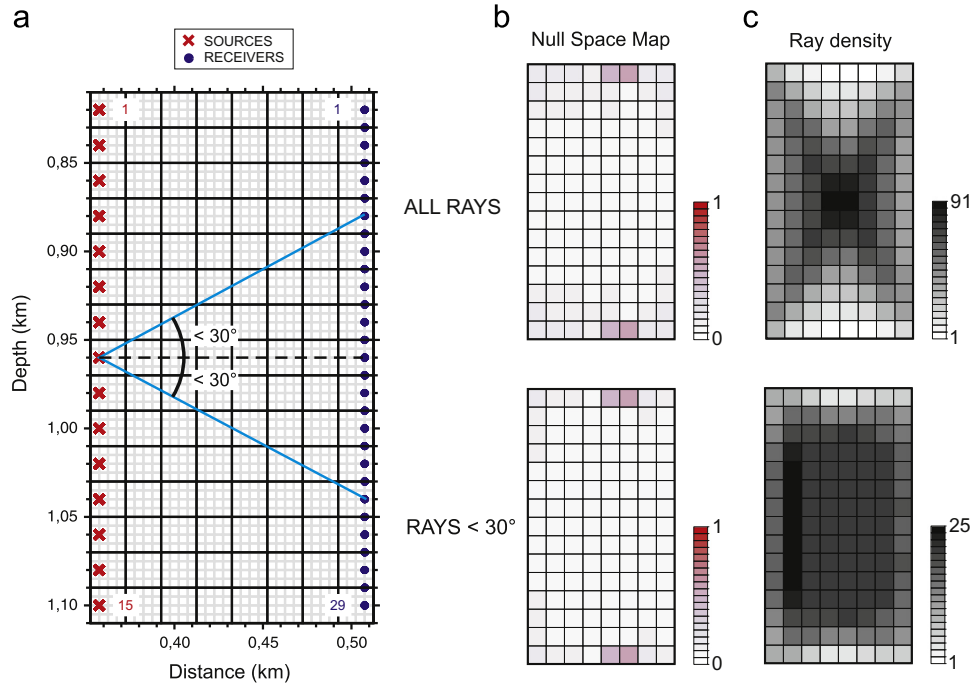


Fig. 3. Tomography grid corresponding to Method 1, where a discretisation of 10×15 squared cells of side 20 m has been used. Also shown are the locations of the sources (crosses) and receivers (dots). The null space and ray density are displayed in Fig. 3b and c, respectively, corresponding to two ray coverages (all the rays and 30° as indicated in Fig. 3a). The grey lines in Fig. 3a define a denser mesh of 32×60 cells as a result of applying the staggered-grid method.

the total mass of CO_2 is about 6.9 Mt. The computed magnetic-field time histories and synthetic seismograms correspond to a cross-hole source–receiver configuration. The wells separation is 160 m, and the source and receiver spacing are 20 m and 10 m, respectively. The total number of sources and receivers is 15 and 29, respectively, covering a depth of 280 m. We obtain traveltime picks (first arrival versus receiver locations) on the synthetic data, which are the basis for electromagnetic and seismic tomography. The computed fields before and after CO_2 injection show the expected differences, i.e., lower traveltimes in the electromagnetic case and higher traveltimes in the seismic case (Carcione et al., 2012). The application of the staggered-grid method allows us a resolution of 5 m for the seismic velocity, quality factor and conductivity fields (Böhm et al., 2000).

We do not consider the effect of a steel casing. However, results from previous works have shown that EM propagation is feasible through casing (Augustin et al., 1989; Wilt et al., 1995; Dodds, 2005; Hu et al., 2008). Wilt et al. (1995) developed a numerical code to calculate the attenuation and phase delay of an EM dipole signal propagating through a steel well casing lodged in a homogeneous medium. They also performed field measurements in an oil field, showing that the casing effect is quite local, most likely due to the pipe immediately surrounding the sensor. Other numerical and scale model results suggest that for distant sources the formation and pipe effects are separable by simple arithmetic means (Augustin and Kennedy, 1988). The steel casing therefore primarily acts as a filter and its effect may be removed by knowing the filter response.

2. Seismic and EM tomography. Basic approach

In the homogeneous case (a uniform medium), the physics of first arrivals (P- and S-waves or diffusion EM waves) is dictated by an equation of the form

$$\frac{\partial^\nu \varphi}{\partial t^\nu} = \gamma \Delta \varphi + s, \quad (1)$$

where $\nu = 1$ and 2 for diffusion and waves, respectively, φ is the wave field, s is a source, γ is related to the physical property to be inverted (see below) and Δ is the Laplacian. The seismic wave field can be the pressure, particle velocity or displacement and the electromagnetic wave field is the electric field or the magnetic field. The differential equations corresponding to the general inhomogeneous case can be found in Carcione et al. (2012).

Traveltime tomography is based on the first arrival at each receiver (e.g., Michelini, 1995). In the seismic case $\gamma = v^2$, where v is the velocity of the wave. The method is based on a discretisation of the model space in pixels or voxels and considers the first arrival as a line integral of the form

$$t_p = \int_{x_1}^{x_2} \frac{dx}{v}, \quad (2)$$

where x_1 and x_2 refer to the source and receiver locations, respectively. The algorithm consist in finding the velocity model that satisfies Fermat's principle, i.e., such that the raypath has the minimum traveltime.

On the other hand, the EM case is less known. Let us consider for illustration the homogeneous case. One version of Eq. (1) can be written as

$$\frac{\partial H}{\partial t} = D \Delta H + M_0 \delta(t) \delta(\mathbf{x}) \quad (3)$$

(e.g., Carcione, 2015), where H is a magnetic field component, M_0 is the source strength and δ is Dirac's function. The diffusivity is given by

$$D = \frac{1}{\mu \sigma} \quad (4)$$

where μ is the magnetic permeability and σ is the electrical conductivity. Here, we assume $\mu = \mu_0 = 4\pi 10^{-7}$ H/m, the magnetic permeability of vacuum.

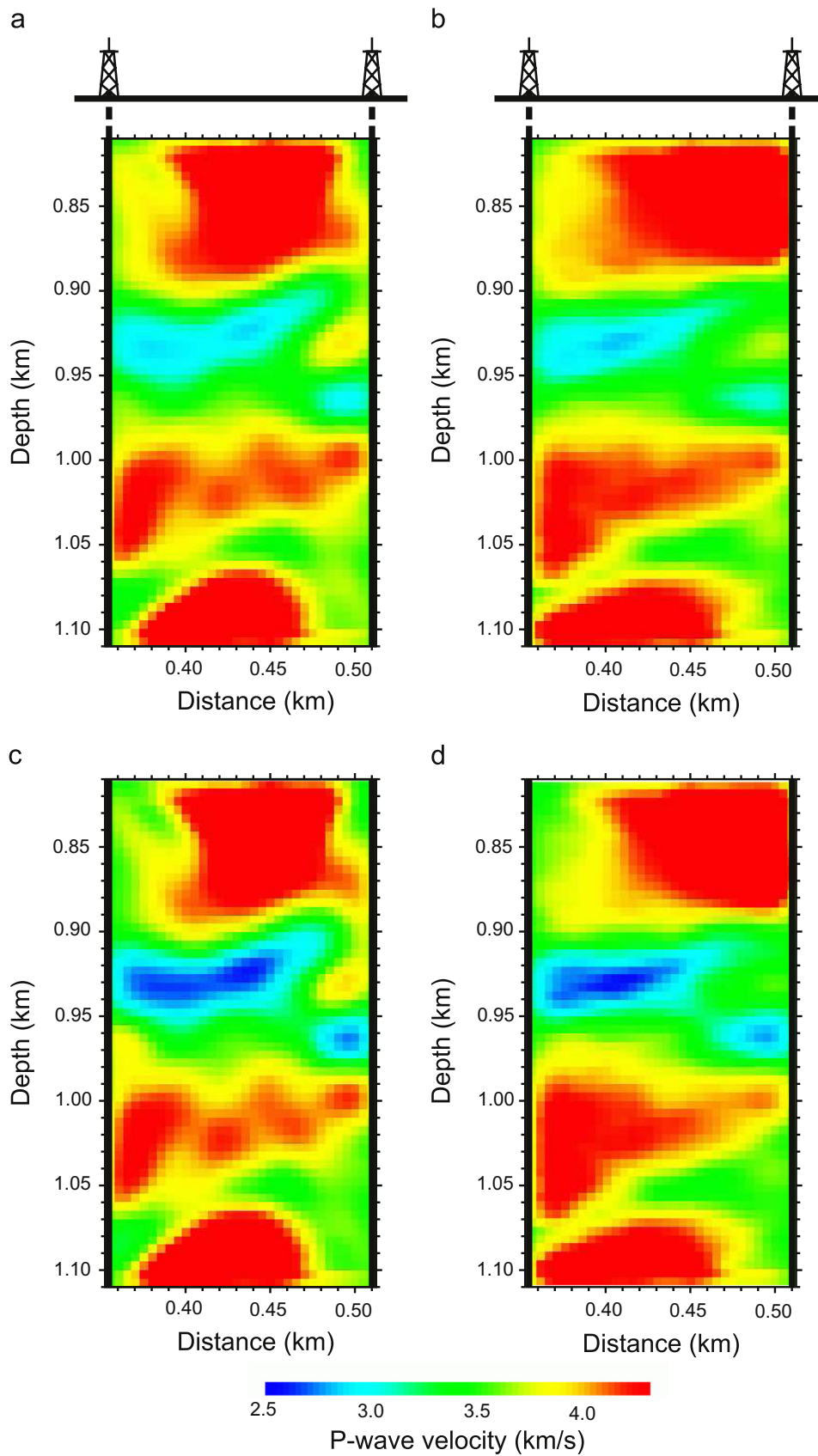


Fig. 4. Pre-injection (a and b) and post-injection (c and d) results from Method 1 with all the rays (a and c) and with 30° coverage (b and d).

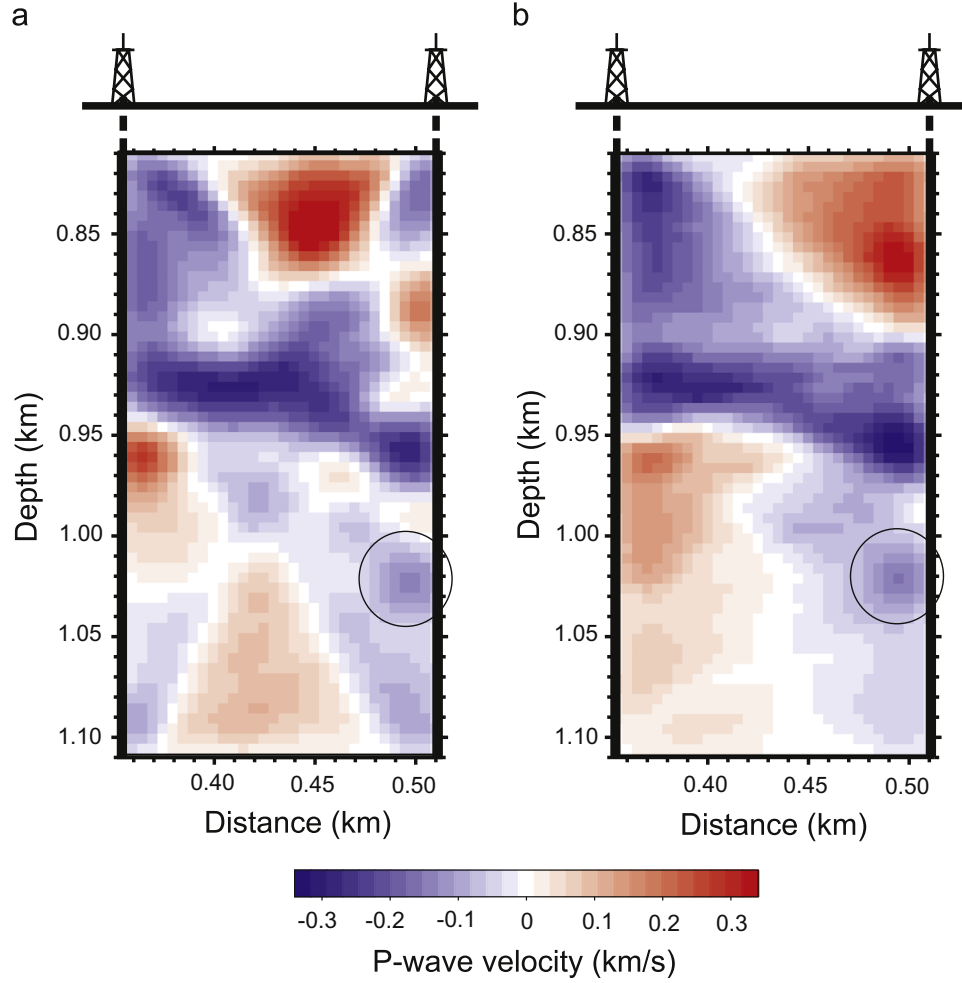


Fig. 5. Post-injection minus pre-injection tomographic seismic velocities obtained with Method 1, corresponding to all the rays (a) and 30° coverage (b).

Eq. (3) has the following solution (Green's function):

$$H(r, t) = \frac{M_0}{(4\pi Dt)^{N/2}} \exp[-r^2/(4Dt)], \quad (5)$$

where N is the space dimension ($N=2$ in this work), and (Carslaw and Jaeger, 1959; Oristaglio and Hohmann, 1984; Carcione, 2015)

$$r = \sqrt{x^2 + z^2}. \quad (6)$$

The solution $H(t)$ has a maximum at

$$t_p = \frac{r^2}{4D} = \frac{\mu\sigma r^2}{4} \quad (7)$$

[$t_p = r^2/(6D)$ in 3D space]. Then, in a homogeneous medium, the conductivity can simply be obtained as $\sigma = 4t_p/(\mu r^2)$, at a source-receiver distance r . Eq. (7) indicates that the diffusion is faster in resistive media. The phase velocity and attenuation factor for plane waves are

$$v = 2\sqrt{\frac{\pi f}{\mu\sigma}} = 2\sqrt{\pi f D} \quad \text{and} \quad \alpha = \sqrt{\pi f \mu\sigma}, \quad (8)$$

respectively, where f is the frequency (e.g., Carcione, 2015; Carcione et al., 2012) and α is the reciprocal of the skin depth. Therefore the penetration is less in more conductive media.

In inhomogeneous media, we need to perform traveltime tomography (e.g., Brauchler et al., 2003; Böhm et al., 2011), which, in 2D space, is based on the following line integral (see Appendix):

$$\sqrt{t_p} = \frac{1}{2} \int_{x_1}^{x_2} \frac{dx}{\sqrt{D}}. \quad (9)$$

In this case, one has to find the diffusivity (or conductivity) model satisfying Fermat's principle, but replacing t with \sqrt{t} being variable. The traveltime is obtained as the time that the first derivative of the field is zero (Yu and Edwards, 1997; Carcione et al., 2012). An alternative picking method is given in Lee and Uchida (2005).

We also perform seismic attenuation tomography. The basic approach to obtain the quality factor Q is the following. As the wave propagates the amplitude decreases, pulse broadening occurs and high frequencies are lost. A measure of the frequency shift of the spectrum is the variation of the spectral content of the pulse, ξ , defined as

$$\xi = \frac{f_s - f_r}{\sigma_s^2}, \quad (10)$$

where f_s and f_r are the centroid frequencies at the source and receiver, respectively, and σ_s^2 is the spectral variance of the initial pulse (Quan and Harris, 1997).

A relation similar to (2) can be established between the spectral content and the attenuation factor α , i.e.

$$\xi = \int_{x_1}^{x_2} \alpha dx, \quad (11)$$

where

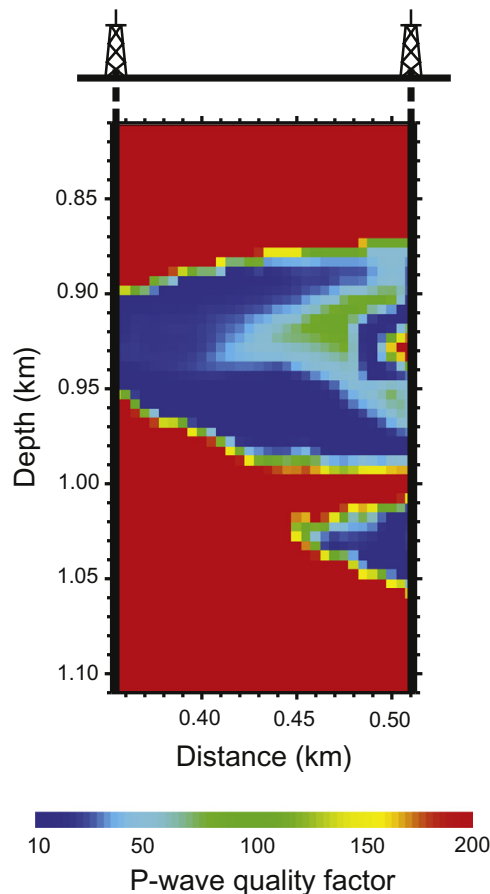


Fig. 6. True post-injection P-wave Q factor map. (For interpretation of the references to colour in this figure caption, the reader is referred to the web version of this paper.)

$$\alpha = \frac{\pi f}{vQ}. \quad (12)$$

The method is illustrated in [Quan and Harris \(1997\)](#) and [Rossi et al. \(2007\)](#).

The CAT3D tomography algorithm, hereafter “Method 1”, computes the traveltimes by a minimum-time ray-tracing algorithm in irregularly shaped homogeneous voxels ([Böhm et al., 2000](#)). The velocities are estimated with the ART and SIRT approaches, followed by a natural smoothing obtained by staggered grids ([Böhm et al., 1999, 2007](#); [Vesnaver and Böhm, 2000](#)). Generally, a first inversion is performed with straight rays (as in medical tomography) to obtain an initial model and then a ray tracing algorithm is used to model curved rays according to Fermat's principle. For Q inversion, the initial model consists of the P-wave velocity from the traveltimes inversion, and the P-wave quality factor, which is constant as a first guess. The velocity information is used only for the ray tracing, whereas the residuals of the spectral content of the seismic pulses are used to improve the Q-model throughout the tomographic iteration.

On the other hand, [Michellini \(1995\)](#) developed an adaptive mesh scheme, where seismic velocities and node positions are determined simultaneously. Rather than adding or removing nodes, [Michellini \(1995\)](#) relocates nodes depending on the desired resolution. The basis functions to describe the 2D velocity field are cubic B-splines. We refer to this algorithm as “Method 2”.

3. Results

The geological model has been built in [Carcione et al. \(2012\)](#)

and consists of a sandstone aquifer with shale intrusions, embedded in a shale formation. Let us first consider the seismic experiment. [Fig. 1](#) shows the P-wave velocity model before (a) and after (b) the CO₂ injection and panel (c) displays the difference between panels (a) and (b). The red part mainly corresponds to the low-permeability shale formation. As can be seen, these differences can be as high as 300 m/s, with the blue color corresponding to zones saturated with CO₂ (see [Carcione et al., 2012](#)). A seismic shot gather, computed from a viscoelastic simulation, is shown in [Fig. 2a](#), where the solid and dashed lines correspond to the pre- and post-injection cases. [Fig. 2b](#) represents the results of the traveltime picks and, in this case, the traveltimes after the injection are higher than the traveltimes of a water saturated aquifer, as expected ([Picotti et al., 2007](#)).

Let us consider Method 1 first. [Fig. 3a](#) shows the tomography grid, where a discretisation of 10 × 15 squared cells of side 20 m has been used. Also shown are the locations of the sources (crosses) and receivers (dots). The null space and ray density are displayed in [Fig. 3b](#) and [c](#), respectively, corresponding to two ray coverages (all the rays and 30° as indicated in [Fig. 3a](#)). The grey lines in [Fig. 3a](#) define a denser mesh of 32 × 60 cells as a result of applying the staggered-grid method. A measure of the reliability of the tomographic inversion is the null space energy, based on the singular-value decomposition of the tomographic matrix (e.g. [Vesnaver and Böhm, 2000](#)). Null space energy values vary from 0 to 1, where 1 is related to an infinite number of solutions that satisfy the system of tomographic equations, and therefore to high unreliability. Thus one may retain regions of the model where the null space is low. On the other hand, the staggered-grid method consists of shifting the mesh, horizontally and vertically, by one-fourth of cell (5 m in this case), performing the inversions (sixteen) and averaging them to obtain the velocity field in a 32 × 60 mesh ([Vesnaver and Böhm, 2000](#)).

[Fig. 4](#) shows the inversion with all the rays (a and c) and with 30° coverage (b and d). The reason why we have considered the last coverage is that rays with angles greater than 30° may generate artefacts due to smearing. In (a–c) we have used 435 traveltimes picks while in (b–d) we have used 215 picks. RMS values corresponding to the difference between the computed and observed traveltimes gave 1.4 and 1.2, respectively, in (a–c) and (b–d). The last case yields better results. The velocity difference between the pre- and post-injection panels is shown in [Fig. 5](#). The results compare well with the difference shown in [Fig. 1c](#). In particular, the small spot at approximately 1025 m depth has been detected by the inversion algorithm.

Next, we consider the inversion of the seismic attenuation with 30° coverage. The P-wave quality factor is determined from a mesoscopic rock-physics theory (e.g., [Carcione, 2015](#)), which provides realistic values of Q as a function of porosity, gas saturation, clay content, fluid viscosity and permeability (see [Carcione et al., 2012](#)). The water-saturated medium is lossless and attenuation is due to wave-induced fluid flow due to the presence of carbon dioxide, i.e., partial saturation. Therefore, there is no loss at the pre-injection stage. [Fig. 6](#) shows the post-injection Q factor map. Blue and light blue correspond to high attenuation. The results are shown in [Fig. 7](#), i.e., the inversion and the difference between the true and computed Q values. The blue colour in [Fig. 7a](#) indicates low Q values or high energy loss, showing that the CO₂ bubble has been located by the inversion algorithm on the basis of the seismic attenuation. The white, light red and light blue zones in [Fig. 7b](#) correspond to a reliable Q inversion. The centroid of the signal spectrum is downshifted from high to low frequencies during the propagation from source to receiver ([Fig. 7c](#)). [Fig. 8](#) shows the seismic inversion results using Method 2, which resemble those obtained with Method 1 (see [Fig. 4](#)).

Time histories of the magnetic field are shown in [Fig. 9a](#), where

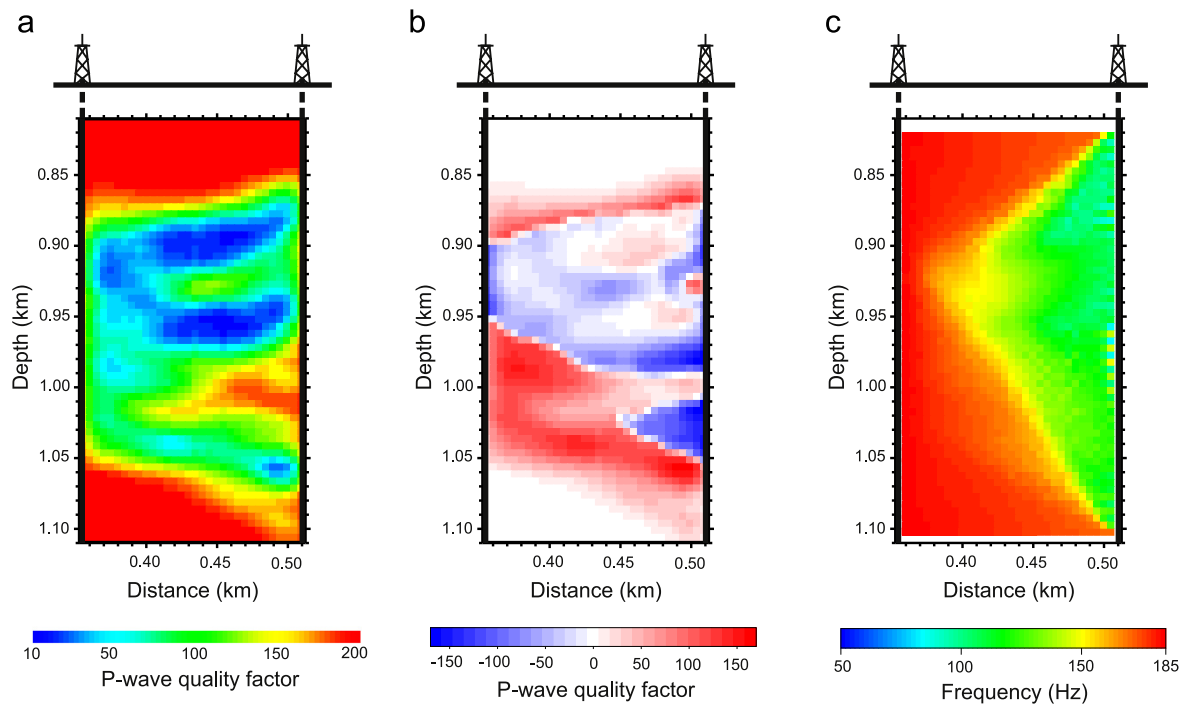


Fig. 7. Post-injection tomographic Q (a), difference between the true values and the computed values (b), and average frequency map (c). (For interpretation of the references to colour in this figure caption, the reader is referred to the web version of this paper.)

the solid and dashed lines correspond to the pre- and post-injection cases. Fig. 9b represents the results of the traveltimes picks and, in this case, the traveltimes after the injection are smaller than the traveltimes of a water saturated aquifer, as expected, due to the higher resistivity of the layers partially saturated with carbon dioxide. The results of the tomography algorithm (Method 1) are given in Figs. 10–12. We obtain the electrical diffusivity, according to Eq. (9), and then calculate the conductivity from Eq. (4) by assuming the magnetic permeability of vacuum, i.e., $\mu_0 = 4\pi \cdot 10^{-7}$ H/m. Fig. 10 corresponds to the true model while Fig. 11 displays the inversion results. The high conductive zone (yellow, see Fig. 11a) disappeared after the injection of CO₂ and the red spot in Fig. 11c reveals the extent of the CO₂ plume clearly. In Fig. 12, the plume area has an average conductivity around zero values indicating the relatively good performance of the inversion algorithm.

In order to evaluate the reliability of Method 1, we computed the RMS (root-mean-square) difference between the inverted models and the true models. The values obtained for the seismic velocity and conductivity before injection are 344 m/s and 0.361 S/m, respectively. Considering all the rays, the RMS velocity value increases to 373 m/s, as expected. The values obtained for the seismic velocity, P-wave quality factor (Q) and conductivity after injection are 426 m/s, 61 and 0.262 S/m, respectively. These values can be considered as an estimation of the error associated to this kind of experiments.

Next, we invert for the petrophysical properties of the aquifer using the results obtained from the tomographic analysis based on Method 1. Since we have the true model (Carcione et al., 2012 and

Fig. 1), this procedure provides a test of the inversion algorithm. The inverse problem is underdetermined if we consider only the seismic velocity and quality factor, because there are three unknowns: CO₂ saturation, S_g , porosity, ϕ , and clay content, C . Incorporating the electrical conductivity, σ removes the indetermination, but the solution requires very efficient optimisation algorithms. We have used the constitutive relations based on the White/CRIM theories given in Sections 2.1, 2.2 and Appendix A of Carcione et al. (2012), where the permeability is related to the clay content and porosity. Because of the complexity of the White model, we adopted a forward optimisation method to minimise the following misfit function:

$$\begin{aligned} & |v(S_g, \phi, C) - v_{\text{tom}}| + C_1 |Q(S_g, \phi, C) - Q_{\text{tom}}| + C_2 \\ & |\sigma(S_g, \phi, C) - \sigma_{\text{tom}}|, \end{aligned} \quad (13)$$

where v_{tom} , Q_{tom} and σ_{tom} are the tomographic velocity, quality factor and electrical conductivity, respectively, and C_1 and C_2 are weighting coefficients. The petrophysical inversion procedure works as follows: for each pixel of the model, we vary S_g , ϕ and C from 0.2% to 98%, using a step rate of 0.1%, to find the global minimum of the misfit function. Considering the size of our model, this simple procedure is quite efficient. Larger models require more efficient optimisation algorithms based, for example, on simulated annealing (Kirkpatrick et al., 1983) or pattern search methods (Griffin et al., 2008).

Fig. 13 shows the original model (a,d,g), the results of the petrophysical inversion (b,e,h), and the corresponding differences (c,f,i). We obtained the best results using $C_1 = 10$ and $C_2 = 1000$, for

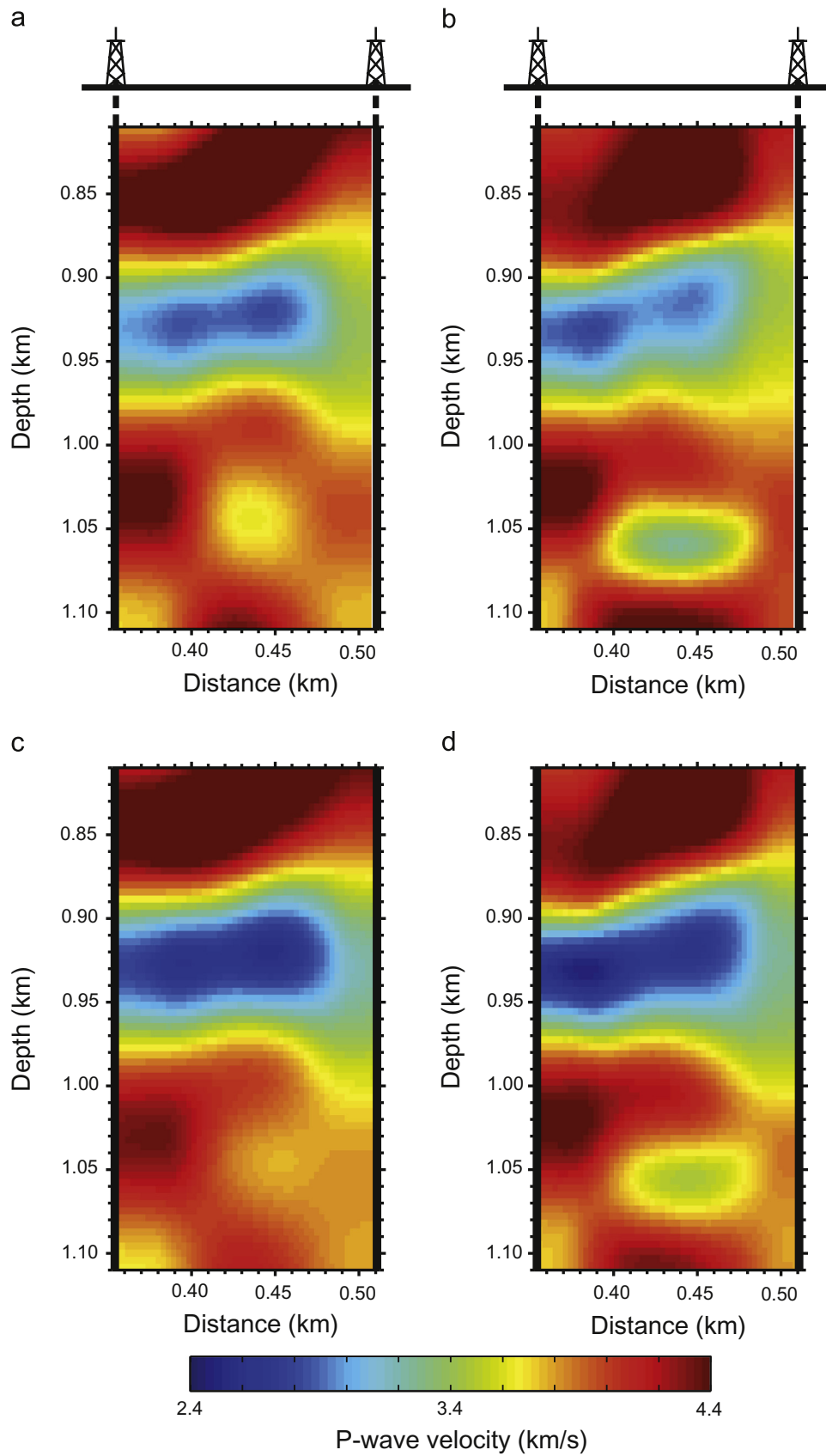


Fig. 8. Pre-injection (a and b) and post-injection (c and d) results from Method 2, using a regular grid (a and c) and an adaptive grid (b and d).

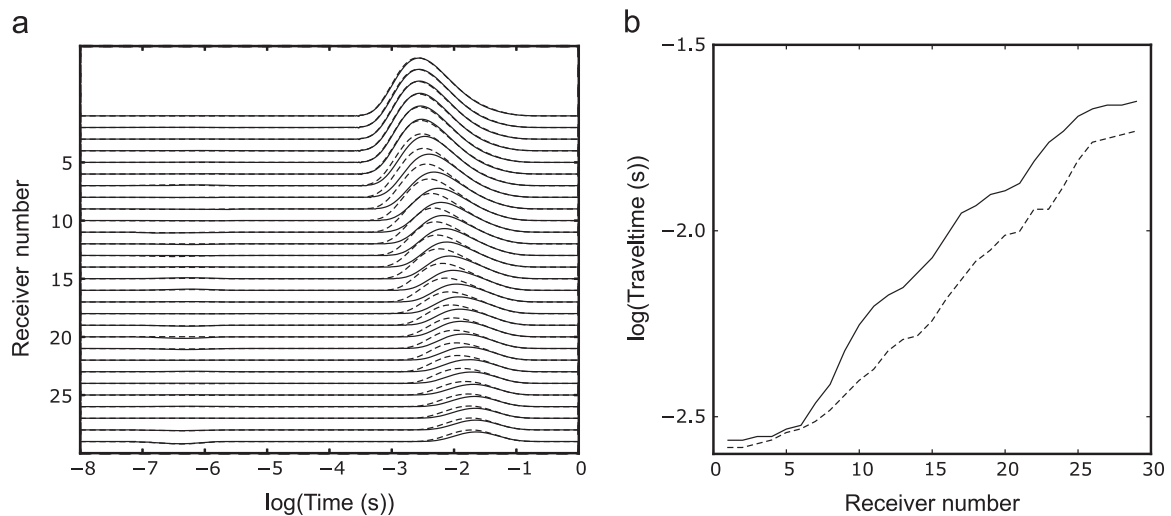


Fig. 9. Normalised EM amplitude variation versus receiver number before and after the injection (solid and dashed curves, respectively) (a), and corresponding traveltime picks (b). The source is located at the left well at a depth of 800 m and the vertical array of receivers is located at the right well (see Fig. 1).

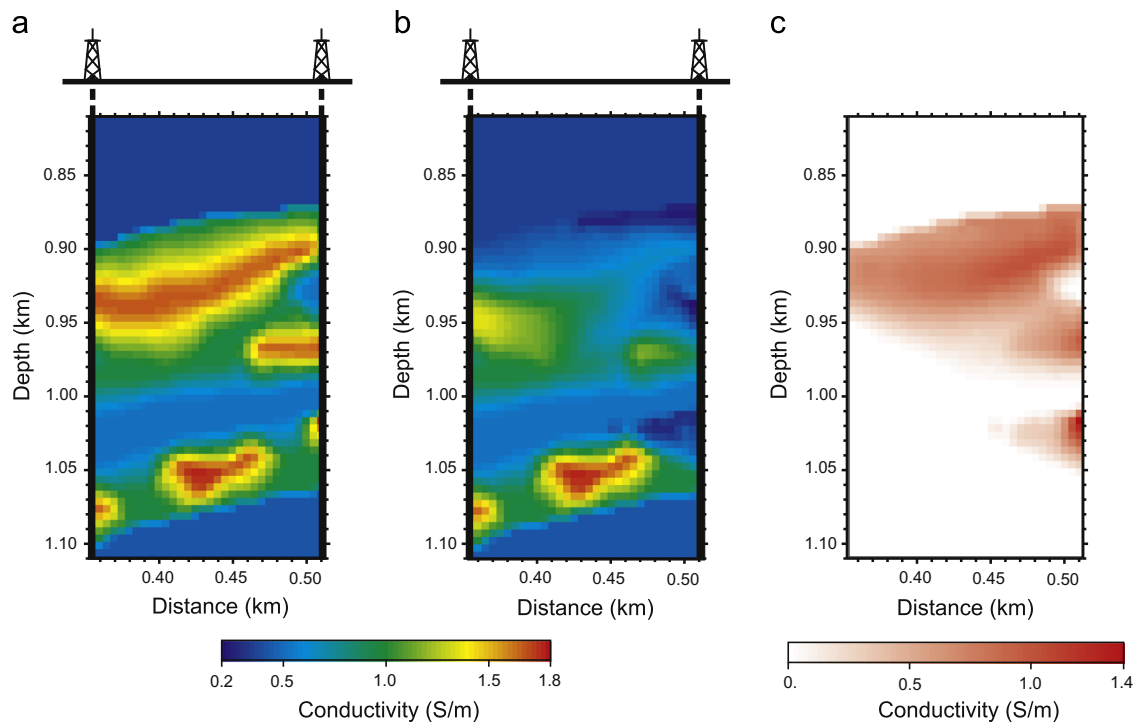


Fig. 10. True electrical conductivity model before (a) and after (b) the CO₂ injection corresponding to the geological model defined in Carcione et al. (2012). Panel (c) shows the difference between panels (a) and (b).

which the three terms of the sum have the same order of magnitude. The saturation model shows that the main CO₂ plume area, indicated by a red box, is well reproduced (b) and the average error is less than 15% (c). The errors are higher in the upper left corner and close to the edges of the model, where the ray coverage is low and the tomographic model is less reliable. Also, the porosity model is well reconstructed inside the red box (e), showing errors lower than 10%, while the high porosity lobe in the lower part of the model is not well recovered. This is caused by the absence of CO₂ in this zone, which reduces the sensitivity of the inversion. Conversely, in the zones where the gas is present we have a strong decrease of the quality factor and the velocity due to the mesoscopic-loss effect, together with an increase of the resistivity, which determine an increase of the sensitivity and a decrease of the errors (f). The clay content model has the largest

errors (i) outside the red box. This is mainly due to the fact that the permeability varies orders of magnitude compared to porosity and saturation. However, it is noticeable that inside the red box, like with porosity and saturation, the errors are lower than 15%, confirming that the presence of gas increases the sensitivity and the reliability of the inversion.

In order to test the effects of noise, we added Gaussian noise to the pre- and post-injection traveltimes by considering only the target zone, i.e., where there is gas. Fig. 14 shows the difference before and after the injection, where the tests yield (a) RMS=181 m/s (no noise); (b) RMS=177 m/s (noise RMS=0.5 ms); (c) RMS=209 m/s (noise RMS=1 ms); and (d) RMS=304 m/s (noise RMS=2 ms). Since the maximum velocity variation is 358 m/s (true models), we may conclude that cases (a)–(c) are acceptable, i.e., an RMS error up to 1 ms. The same

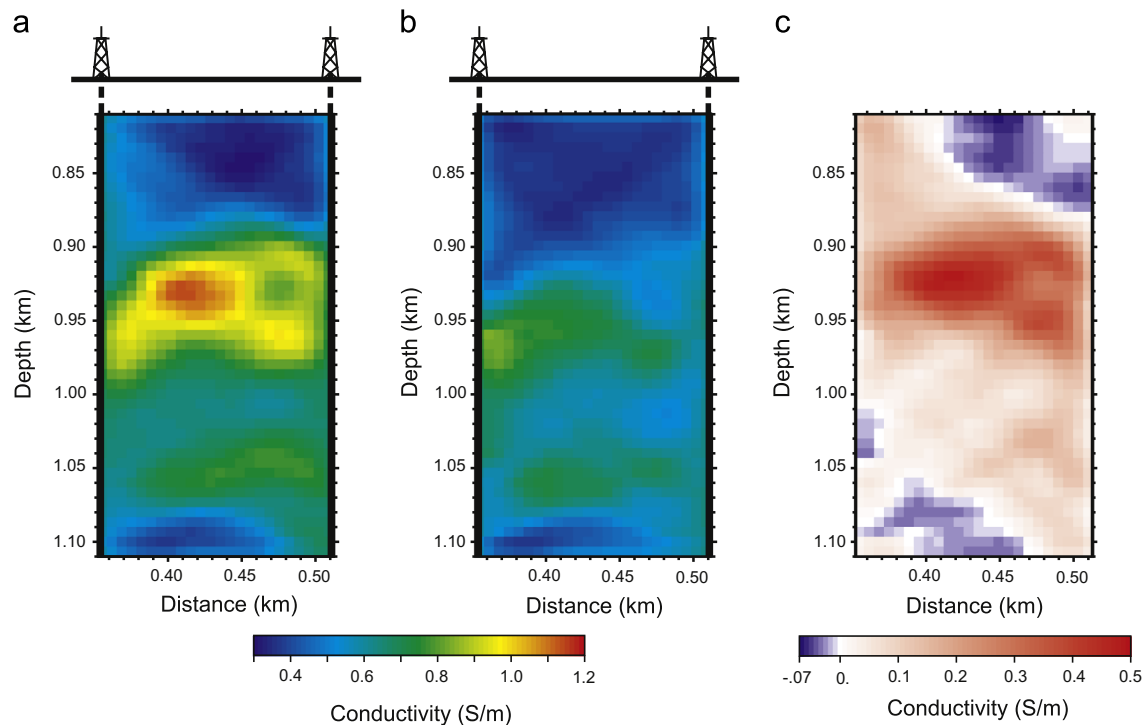


Fig. 11. Inversion results of the electrical conductivity before (a) and after (b) the injection. Panel (c) shows the difference between panels (a) and (b). (For interpretation of the references to colour in this figure caption, the reader is referred to the web version of this paper.)

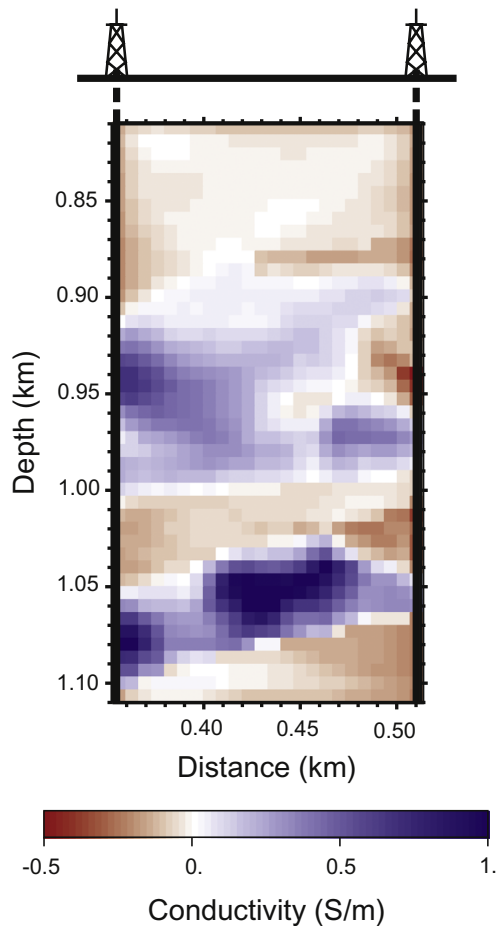


Fig. 12. Difference between the true electrical conductivity and tomographic-inversion results after the injection.

analysis applies to the EM case, which shows a similar wave-like behavior in the log-time scale. On the other hand, regarding attenuation tomography, Picotti and Carcione (2006) tested the reliability of the spectral-ratio and frequency-shift methods for estimating the intrinsic quality factor Q in the presence of random noise. The two methods are very accurate (deviations less than 5% for $Q=100$) and equivalent when in the presence of low values of noise levels (S/N ratio of 20 dB). Moreover, the frequency-shift method is better than the spectral-ratio method when the noise level is high (deviations less than 12% for $Q=100$ and S/N=6 dB).

The procedure present here could be improved by using full waveform inversion after traveltimes and attenuation tomography. For cross-well data, Zhang (2013) has shown that waveform tomography is effective for the CO₂ injection monitoring at the Ketzin site. For surface data, this method does not recover the true value of the velocity anomaly due to the injection, but it qualitatively locates the distribution of the plume. Another improvement could be obtained by using the double-difference waveform inversion which inverts the difference in the model that causes the waveform changes between the baseline and repeat data (e.g., Yang et al., 2011).

4. Conclusions

Time-lapse or 4D techniques are based on the difference between geophysical surveys to measure production and reservoir properties during the life of a reservoir. In this work, differences in seismic velocity and Q and electrical conductivity allow us to detect the presence of CO₂ after its injection. The success is subject to the performance of an inversion algorithm able to discriminate between brine and CO₂ partially saturated zones, and finally, to a proper description of the physical properties of the CO₂ bearing rocks, in order to obtain the saturation. The inversion algorithms used here are based on traveltimes tomography, and attenuation tomography to obtain the seismic Q . The electromagnetic surveys

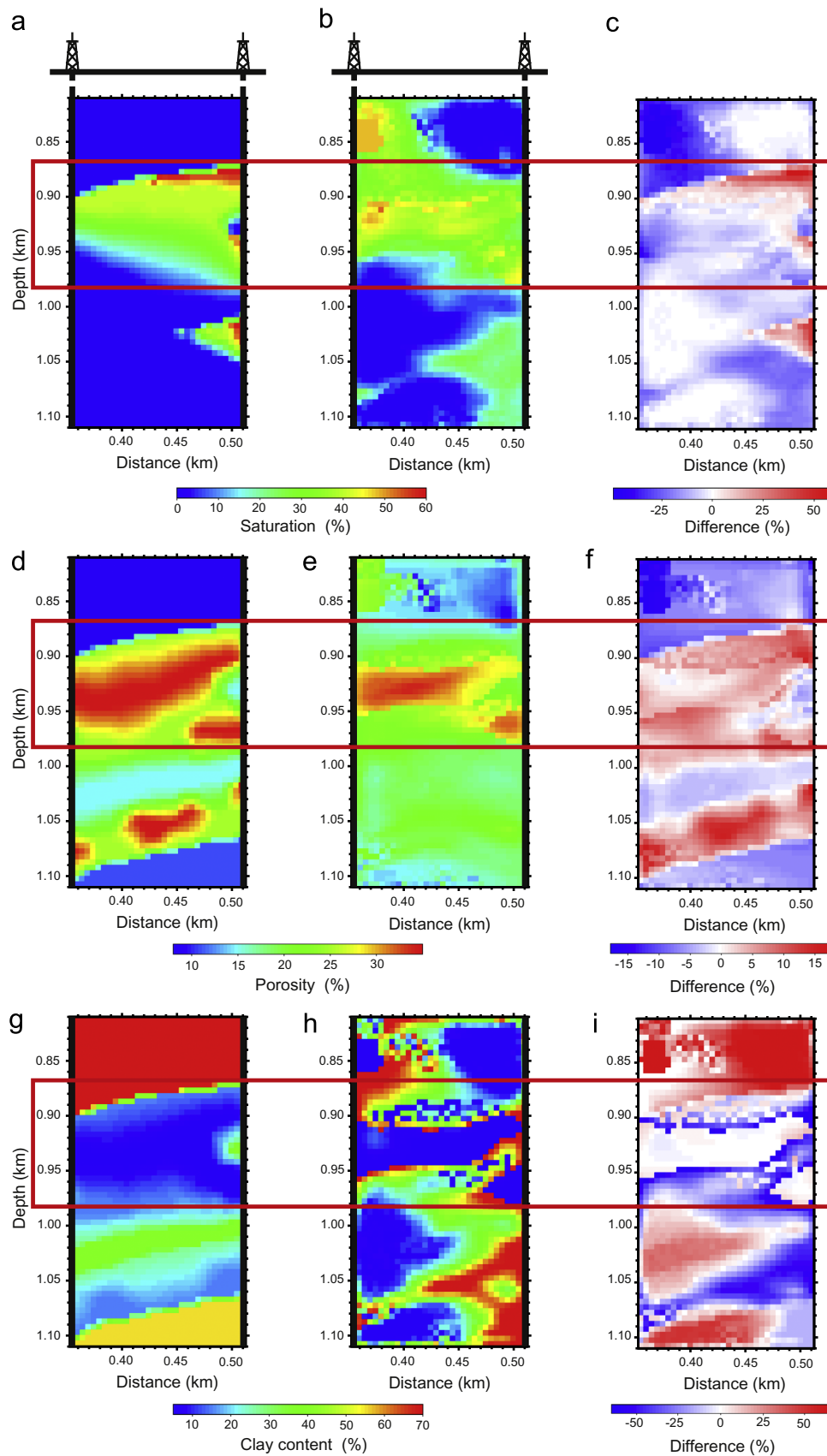


Fig. 13. Aquifer geological model (a,d,g) generated in [Carcione et al. \(2012\)](#), results of the petrophysical inversion (b,e,h), and corresponding differences (c,f,i). (For interpretation of the references to colour in this figure caption, the reader is referred to the web version of this paper.)

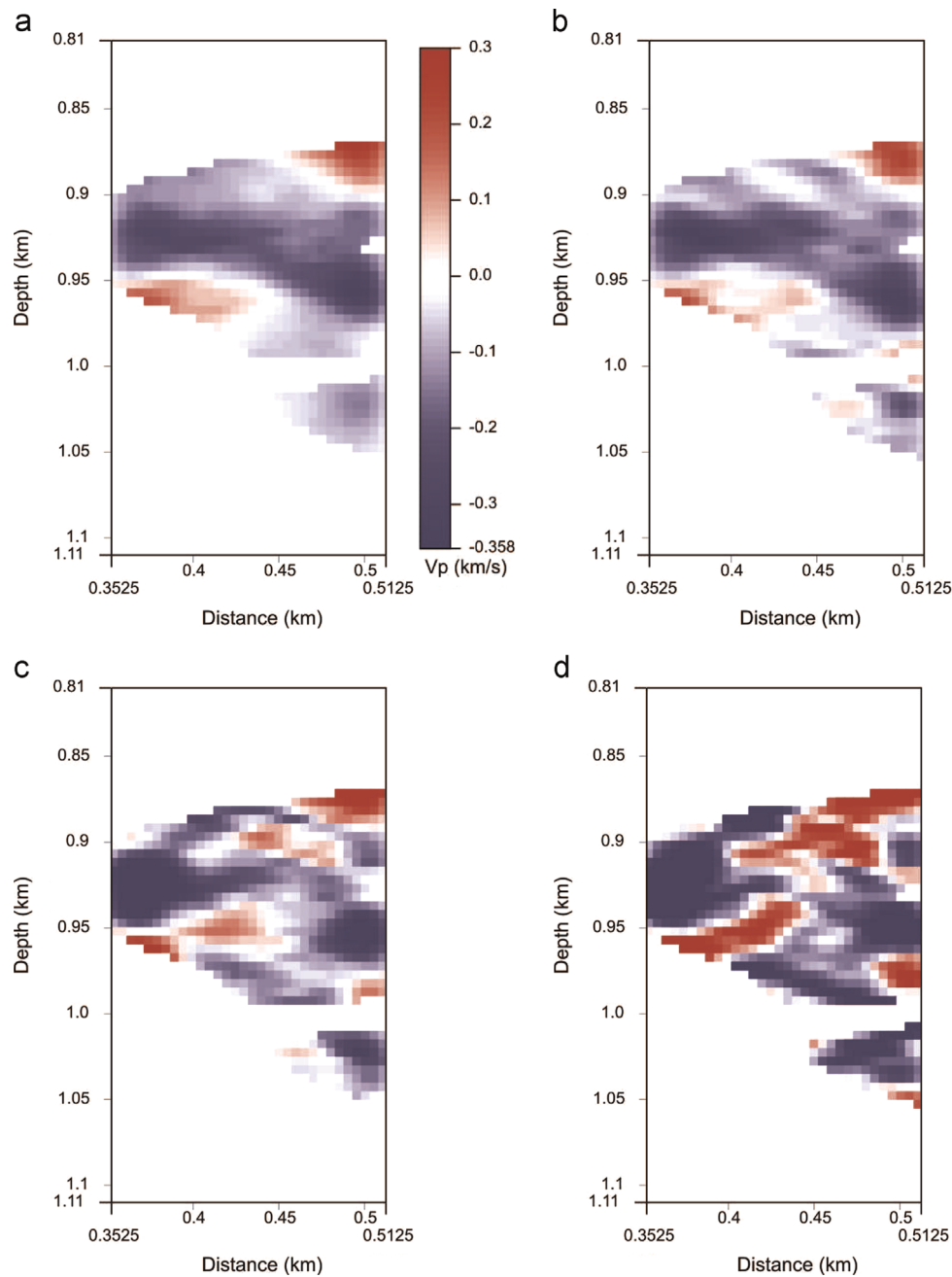


Fig. 14. Analysis of the effects of noise in the traveltimes (Method 1). The panels show the difference between the tomographic velocities before and after the injection (compare to Fig. 1c). The tests correspond to (a) RMS=181 m/s (no noise); (b) RMS=177 m/s (noise RMS=0.5 ms); (c) RMS=209 m/s (noise RMS=1 ms); (d) RMS=304 m/s (noise RMS=2 ms).

have a transient nature and we exploit the fact that the field resembles a wave when represented as a function of the logarithm of time. In this case, it is possible to determine the maximum amplitude and pick the corresponding traveltimes. We have obtained reliable results which agree well with the true petro-physical model.

The computed seismic velocities and Q values can be related to CO_2 saturation, porosity and clay content. Moreover, inverting for the electrical diffusivity allows us to obtain the electrical conductivity and therefore those properties using a suitable rock-physics description of the hosting rock. In this sense, we have computed saturation, porosity and clay content using the results obtained from the tomographic analysis. The forward optimisation method used for the inversion yields errors less than 15%. The saturation and porosity values obtained with these two

approaches can be used to establish cross-property relations between seismic and electromagnetic properties and reduce the cost of geophysical surveys.

It is important to point out that the procedure is suitable for small-scale areas such as those of reservoir geophysics, to monitor reservoir changes between wells during production (oil industry). It is useful where sufficient wells are available and combined with surface based 3D seismic surveys allowing to extrapolate the results over the reservoir scale. Further research involves the use of full-waveform inversion after traveltimes-attenuation tomography, and the implementation of the double-difference waveform inversion.

Acknowledgement

This work has been supported by the CO2Monitor, CO2CARE and Quest projects. We thank two anonymous reviewers for useful comments.

Appendix A. EM travelttime-tomography equation

Consider Eq. (3) and perform a transform from the time domain to the Q -domain,

$$\frac{\partial^2 H}{\partial q^2} = D\Delta H + M_0 \delta(q) \delta(\mathbf{x}), \quad (14)$$

where $q = \sqrt{t}$ and

$$H(r, t) = \frac{1}{2\sqrt{\pi}t^3} \int_0^\infty q \exp\left(-\frac{q^2}{4t}\right) H(r, q) dq \quad (15)$$

is the transform (Lee and Xie, 1993). Eq. (14) is a wave equation with velocity

$$v = \sqrt{D} \quad (16)$$

(the unit is $[m/\sqrt{s}]$). On the other hand, it can easily be shown that the Green function (5) has a peak at

$$t = \frac{r^2}{2ND} = \frac{r^2}{2Nv^2}. \quad (17)$$

Then

$$\sqrt{t} = \frac{r}{\sqrt{2N}v}, \quad (18)$$

which is the relation to be used for travelttime-tomography inversion.

References

- Arts, R., Eiken, O., Chadwick, R.A., Zweigel, P., Van der Meer, L., Zinsner, B., 2004. Monitoring of CO₂ injected at Sleipner using time-lapse seismic data. *Energy* 29, 1383–1392.
- Augustin, A.M., Kennedy, W.D., 1988. A theoretical study of surface-to-borehole electromagnetic logging in cased holes. *Geophysics* 54, 90–99.
- Augustin, A. M., W.D.Kennedy, H. F. Morrison, and K. H. Lee, 1989, A theoretical study of surface-to-borehole electromagnetic logging in cased holes: *Geophysics*, 54, 90–99.
- Best, A.I., McCann, C., Sothcott, J., 1994. The relationships between the velocities, attenuations and petrophysical properties of reservoir sedimentary rocks. *Geophys. Prospect.* 42, 151–178.
- Böhm, G., Brauchler, R., Nieto, D., Soncin, G., Baradello, L., Pivetta, M., Botti, B., 2011. Experimental correlations between geophysical and hydraulic parameters from different inversion procedures. In: 17th European Meeting of Environmental and Engineering Geophysics.
- Böhm, G., Galuppo, P., Vesnaver, A., 2000. 3D adaptive tomography using Delaunay triangles and Voronoi polygons. *Geophys. Prospect.* 48, 723–744.
- Böhm, G., Ocakoglu, N., Picotti, S., 2007. Seismic investigation and 3D tomography in the Ross Sea (Antarctica) for western ice sheet evolution studies. In: 69th EAGE Conference & Exhibition, Extended Abstract C045.
- Böhm, G., Rossi, G., Vesnaver, A., 1999. Minimum time ray-tracing for 3-D irregular grids. *J. Seism. Explor.* 8, 117–131.
- Bourgeois, B., Rohmer, J., Girard, J.-F., 2009. Numerical modelling of the time-lapse EM response of a CO₂ injection in a deep saline aquifer using metallic casings for the current injection. In: AAPG/SEG/SPE Hedberg Conference, “Geological carbon sequestration: Prediction and verification”, Vancouver, Canada.
- Brauchler, R., Liedl, R., Dietrich, P., 2003. A travel time based hydraulic tomographical approach. *Water Resour. Res.* 39, 1370. <http://dx.doi.org/10.1029/2003WR002262>.
- Carcione, J.M., 2015. *Wave Fields in Real Media. Theory and Numerical Simulation of Wave Propagation in Anisotropic, Anelastic, Porous, and Electromagnetic Media*, 3rd edition. Elsevier, Amsterdam.
- Carcione, J.M., Gei, D., Picotti, S., Michelini, A., 2012. Cross-hole electromagnetic and seismic modeling for CO₂ detection and monitoring in a saline aquifer. *J. Pet. Sci. Eng.* 100, 162–172.
- Carcione, J.M., Helle, H.B., Pham, N.H., 2003. White’s model for wave propagation in partially saturated rocks: comparison with poroelastic numerical experiments. *Geophysics* 68, 1389–1398.
- Carcione, J.M., Picotti, S., 2006. P-Wave seismic attenuation by slow-wave diffusion: effects of inhomogeneous rock properties. *Geophysics* 71, O1–O8.
- Carcione, J.M., Picotti, S., Gei, D., Rossi, G., 2006. Physics and seismic modeling for monitoring CO₂ storage. *Pure Appl. Geophys.* 163, 175–207.
- Carcione, J.M., Ursin, B., Nordskog, J.L., 2007. Cross-property relations between electrical conductivity and the seismic velocity of rocks. *Geophysics* 72, E193–E204.
- Carslaw, H.S., Jaeger, J.C., 1959. *Conduction of Heat in Solids*. Clarendon Press, Oxford.
- Christensen, N.B., Sherlock, D., Dodds, K., 2006. Monitoring CO₂ injection with cross-hole electrical resistivity tomography. *Explor. Geophys.* 37, 44–49.
- Dodds, K., 2005. Time-lapse EM and seismic imaging of a CO₂ plume. Presented at the National Energy Technology Laboratory Fourth Annual Conference on Carbon Capture and Sequestration. Alexandria, Virginia, May 2–5, 2005. GCCC Digital Publication Series #05-04, pp. 1–35.
- Griffin, J.D., Kolda, T.G., Lewis, R.M., 2008. Asynchronous parallel generating set search for linearly-constrained optimization. *SIAM J. Sci. Comput.* 30, 1892–1924.
- Helle, H.B., Pham, N.H., Carcione, J.M., 2003. Velocity and attenuation in partially saturated rocks: poroelastic numerical experiments. *Geophys. Prospect.* 51, 551–566.
- Hu, W., Xu, Z., Yan, L., Wang, J., Strack, K.M., Yu, G., 2008. Model study on through casing time domain electromagnetic (TEM) probing. In: Proceedings of the 2008 SEG Annual Meeting, Society of Exploration Geophysicists, Las Vegas.
- Kirkpatrick, S., Gelatt, C.D., Vecchi, M.P., 1983. Optimization by simulated annealing. *Science* 220.
- Lee, T.J., Uchida, T., 2005. Electromagnetic travelttime tomography: application for reservoir characterization in the Lost Hills oil field, California. *Geophysics* 70, G51–G58.
- Lee, K.H., Xie, G., 1993. A new approach to imaging with low frequency electromagnetic fields. *Geophysics* 58, 780–796.
- Michelini, A., 1995. An adaptive-grid formalism for travelttime tomography. *Geophys. J. Int.* 121, 489–510.
- Norman, T., Alnes, H., Christensen, O., Zach, J.J., Eiken, O., Tjaland, E., 2008. Planning time-lapse CSEM-surveys for joint seismic-EM monitoring of geological carbon dioxide injection. In: EAGE CO₂ Geological Storage Workshop, Budapest, Hungary.
- Oristaglio, M.L., Hohmann, G.W., 1984. Diffusion of electromagnetic fields into a two-dimensional earth: a finite-difference approach. *Geophysics* 49, 870–894.
- Picotti, S., Carcione, J.M., 2006. Estimating seismic attenuation (Q) in the presence of random noise. *J. Seism. Explor.* 15, 165–181.
- Picotti, S., Carcione, J.M., Rubino, J.G., Santos, J.E., 2007. P-wave seismic attenuation by slow-wave diffusion: numerical experiments in partially saturated rocks. *Geophysics* 72 (4), N11–N21. <http://dx.doi.org/10.1190/1.2740666>.
- Picotti, S., Carcione, J.M., Gei, D., Rossi, G., Santos, J.E., 2012. Seismic modeling to monitor CO₂ geological storage—The Atzbach–Schwanenstadt gas field. *J. Geophys. Res.: Solid Earth* 117 (6), B06103. <http://dx.doi.org/10.1029/2011JB008540>.
- Picotti, S., Grünhut, V., Osella, A., Gei, D., Carcione, J.M., 2013. Sensitivity analysis from single-well ERT simulations to image CO₂ migrations along wellbores. *The Leading Edge*, May Issue, 504–512.
- Quan, Y., Harris, J.M., 1997. Seismic attenuation tomography using the frequency shift method. *Geophysics* 62, 895–905.
- Rossi, G., Gei, D., Böhm, G., Madrusani, G., Carcione, J.M., 2007. Attenuation tomography: an application to gas-hydrate and free-gas detection. *Geophys. Prospect.* 55, 655–669.
- Saito, H., Nobuoka, D., Azuma, H., Xue, Z., Tanase, D., 2006. Time-lapse crosswell seismic tomography for monitoring injected CO₂ in an onshore aquifer, Na-gaoka, Japan. *Explor. Geophys.* 37, 30–36.
- Vesnaver, A., Böhm, G., 2000. Staggered or adapted grids for seismic tomography? *The Leading Edge* 19, 944–950.
- Wilt, M.J., Alumbaugh, D.L., Morrison, H.F., Becker, A., Lee, K.H., Deszcz-Pan, M., 1995. Crosswell electromagnetic tomography—system design considerations and field results. *Geophysics* 60, 871–885.
- Xue, Z., Kim, J., Mito, S., Kitamura, K., Matsuoka, T., 2009. Detecting and monitoring CO₂ with P-wave velocity and resistivity from both laboratory and field scales. In: The SPE International Conference on CO₂ Capture, Storage and Utilization.
- Yang, D., Fehler, M., Malcolm, A., Huang, L., 2011. Carbon sequestration monitoring with acoustic double-difference waveform inversion: a case study on SACROC walkaway VSP data. 2011 SEG Technical Program, Expanded Abstract.
- Yu, L., Edwards, R.N., 1997. On crosswell diffusive time-domain electromagnetic tomography. *Geophys. J. Int.* 130, 449–459.
- Zhang, F., 2013. Quantifying the seismic response of underground structures via seismic full waveform inversion: Experiences from case studies and synthetic benchmarks. *Acta Universitatis Upsaliensis. Digital Comprehensive Summaries of Uppsala Dissertations from the Faculty of Science and Technology* 1005, Uppsala, 62 pp. ISBN 978-91-554-8562-7.